Improved estimation of hourly direct normal solar irradiation (DNI) using geostationary satellite visible channel images over moderate albedo areas

A. Laguarda*, R. Alonso-Suárez, G. Abal

Laboratorio de Energía Solar, Facultad de Ingeniería, UDELAR, J. H. y Reissig 565, CP 11700, Montevideo, Uruguay.

Abstract

An accurate knowledge of the direct solar irradiance at normal incidence (DNI) is required to size solar energy systems, specially those using solar concentration technologies. In the absence of measurements, DNI can be estimated over an arbitrary site with a dedicated satellite model or by using satellite-derived global horizontal irradiance (GHI) and a phenomenological diffuse-direct separation model. This second procedure is error-prone, specially under partial cloudiness conditions and low solar elevation angles. A novel and simple semi-empirical satellite-based model to estimate DNI in moderate albedo regions using a physical clear sky model and a cloudiness index obtained from visible satellite imagery is proposed and assessed. An ergodic assumption in which the images are spatially averaged to better represent the hourly time basis is used. Over the target region (Southeastern South America, SESA), the new DNI satellite model outperforms the alternative strategy at the hourly level, with an average uncertainty of 20% (versus 25%) when compared with three measurement station's data sets located in center Argentina, southern Brazil and Uruguay.

Keywords: Solar radiation, Direct normal irradiance, satellite modeling, semi-empirical model, GOES-East images

1. Introduction

Direct normal solar irradiance (DNI) is the portion of solar radiation that reaches the ground from a small solid angle around the Sun (circumsolar region). It is the most relevant variable required to evaluate the technical and economical feasibility of concentration of solar power (CSP) projects. It is also required to estimate global solar irradiance on inclined surfaces from global horizontal irradiance (GHI), and ultimately, the expected PV power production.

DNI is measured with a pyrheliometer mounted on a precision solar tracker. However, this implies high costs and maintenance requirements and makes long measurement series of DNI relatively scarce. In absence of local quality ground measurements, DNI can be estimated from GHI (satellite-derived or ground

*Corresponding author: A. Laguarda, agu.laguarda@gmail.com

measured) by using diffuse fraction models, (f_d = DHI/GHI), where DHI is the diffuse horizontal irradiance. Phenomenological parameterizations for f_d are usually associated with significant errors (Gueymard and Ruiz-Arias, 2016) even if trained with local data (Abal et al., 2017). Furthermore, this method is not adequate for DNI estimation at low Sun angles as the error is amplified by the $1/\sin\alpha_s$ factor, where α_s is the solar altitude.

An alternative form of estimating DNI is to use a satellite-based model that includes the relevant information on the state of the atmosphere. Heliosat-4 (Qu et al., 2017) is the last-reported Heliosat family model, based on the Meteosat satellite images and other remote-sensed or modeled information. It is a physically motivated model that estimates GHI and DNI for all sky conditions based on two look up tables (LUT) schemes that model the clear sky radiation (Lefèvre et al., 2013) and cloud effects. These LUT result from a Radiative Transfer Model (RTM) with several combinations of atmospheric and cloud conditions. Another family are the SUNY models (Perez et al., 2015). They use GOES satellite information to estimate solar radiation over the Americas with an empirical parametrization of cloud effects. In the past years, the National Solar Radiation Database (NSRDB, https://nsrdb.nrel.gov/) has developed a model to estimate DNI with focus on North America based on RTM parametrizations (Sengupta et al., 2014a,b, 2018; Xie et al., 2016). Recently, some physical improvements were applied to consider the contribution of circumsolar radiation on the Sun-observer direction on the DNI component (Xie et al., 2020). Regarding South America, (Porfirio and Ceballos, 2017) presented a DNI satellite model based on visible channel GOES-East information. The model is built from physical considerations and calculates DNI over Brazil using atmospheric information from different sources.

Previous assessments for satellite-based DNI models at the hourly level, as summarized in Table 1, show that satellite-based estimation of DNI has typically a relative root mean square deviations (rRMSD) with a lower bound around 30% (in terms of the average DNI)[1]. This is significantly larger than the corresponding bound for GHI estimation models which can be as low as 12% of the mean hourly GHI (Laguarda et al., 2020), depending on the site. These results are not to be used to rank models according to performance, since the accuracy of a DNI model depends on local conditions and on the quality of the atmospheric inputs, among other factors. However, Table 1 provides context and shows that there is room for improvement in satellite-based DNI estimation.

In this article, a simple operational model to estimate DNI from visible channel satellite information is presented and assessed. Visible channel images provide daylight cloud information suitable for satellite-based solar radiation models. Cloud detection from the visible channel fails when the target pixel has a high albedo, since clouds can not be distinguished from the bright background. Thus, the model in its present

[1]All the statistical performance metrics used in this work are defined in the usual form (Gueymard, 2014) and are expressed in relative terms as a percentage of the measured variable.

[2]Estimates DNI from the diffuse separation algorithm proposed by Liu and Jordan (1960).

	Performance of satellite-derived hourly DNI			
Model	**rMBD**	**rRMSD**	**sites of validation**	**reference**
SUNY-v1	-4.1	35.1	10 sites en USA	Perez et al. (2002)
SUNY-v1	-18.0	52.0	8 sites en USA	Perez et al. (2015)
SUNY-v2	-2.4	29.9	10 sites en USA	Perez et al. (2002)
SUNY-v2	+6.8	31.0	4 sites en California	Nonnenmacher et al. (2014)
SUNY-v2	-2.5	48.0	8 sites en USA	Perez et al. (2015)
SUNY-v3	+14.3	67.2	3 sites en Canada	Djebbar et al. (2012)
SUNY-v3	+3.5	38.0	8 sites en USA	Perez et al. (2015)
SUNY-v4	-0.5	33.0	8 sites en USA	Perez et al. (2015)
SolarGIS	-2.0	34.1	18 sites en Europe	Ineichen (2014)
NSRDB(v2)	+4.5	33.2	9 sites en USA	Habte et al. (2017)
Heliosat-3[2]	+6.0	47.4	18 sites in Europe	Ineichen (2014)
Heliosat-4	+0.5	28.0	France, Switzerland	`www.soda-pro.com/web-services`
Heliosat-4	0.0	39.0	Florianópolis	`www.soda-pro.com/web-services`

Table 1: Averaged performance Metrics (in % of the mean) reported for hourly satellite-derived DNI.

form is not adequate for areas with significant snow cover or other high albedo surfaces, such as desert areas or salt flats. As a concrete example, we implement the model using publicly available images from the visible channel of the geostationary satellite GOES-East (administrated by the National Oceanic and Atmospheric Administration, NOAA) and test it against hourly ground data for three sites in Southeastern South America (SESA region, (Bettolli et al., 2021; Hu et al., 2022)), a region mostly covered by grasslands without significant elevations and with low-moderate surface albedo.

The method can be potentially applied to other sites for which visible-channel geostationary satellite images are available and provided the target area has a moderate albedo. The model is based on the cloud index strategy originally proposed by Cano et al. (1986) for GHI estimation and later adopted by various authors such as Perez et al. (2002); Rigollier et al. (2004); Laguarda et al. (2020). In this scheme, the ground irradiance is a fraction of the corresponding clear sky irradiance, as estimated with a suitable clear sky model. The effect of clouds is taken into account with an attenuation factor which can be modeled from visible channel images of a geostationary satellite. The implicit assumption that the clear sky modeling and the cloud attenuation are independent instances, has a performance cost that has been quantified with root mean deviations (RMSD) between 2 and 5% of the average DNI (on a one-minute timescale) (Oumbe et al., 2014; Xie et al., 2016). However, the gain provided by this assumption in terms of simplicity and computational requirements compensate this cost, when compared to detailed radiative transfer calculations. Each satellite image quantifies cloudiness through a dimensionless cloudiness index η. Under arbitrary conditions of cloudiness, the attenuation of radiation (with respect to clear sky conditions) is empirically parameterized as a function of η in a form that is only weakly site-dependent, a feature that should be checked over the area of application. Models of this type are generically called Cloud Index Models or CIM. A CIM for GHI has recently been implemented by our group for the SESA region, obtaining an excellent accuracy in terms of rRMSD, of 12% at the hourly level and 15% of the mean at the 10-minute timescale (Laguarda et al., 2020, 2021). The present work extends these developments to the estimation of DNI.

2. Information base

The CIM model described in Section 3 is implemented and evaluated using ground data from three sites representative of the SESA region (see Figure 1). This area has an approximate surface of 1500 km^2, is widely populated, and has an intense socioeconomic activity associated with food production and cattle rising. This territory is geographically homogeneous and composed mainly of low-altitude grasslands (below 1500 m above mean sea level) and snow events are very exceptional. The area includes the territory of Uruguay, southern Brazil and eastern Argentina. Its climate is temperate with hot summers without dry seasons, being classified as Cfa in the updated Köppen-Geiger classification scheme (Peel et al., 2007; Beck et al., 2018). The solar irradiance short-term variability of the region is intermediate (Alonso-Suárez et al., 2020), in which clear, partly cloudy and overcast sky conditions alternate. In this section, the details of the used ground and satellite information are provided.

2.1. Ground Measurements

Ground measurements for GHI and DNI from three sites with the coordinates and data periods listed in Table 2 are used. The equipment and protocols of the three sites meet the quality requirements of the Baseline Surface Radiation Network (McArthur, 2005) although only the SM site (São Martinho da Serra, a site of the SONDA radiometric network, Brazil) is formally a part of BSRN. The other two are the main station of the Solar Energy Laboratory (LES) network at Salto, Uruguay (site code: LE) and the laboratory site of the Gersolar research center, National University of Luján, located 50 km from Buenos Aires, Argentina (site code: LU). At all sites, GHI is measured with class A spectrally flat pyranometers (according to ISO 9060:2018 standard) with ventilation units, while DNI is measured using Kipp & Zonen CHP1 pyrheliometers mounted on precision solar trackers. The instruments are cleaned and visually inspected on a weekly basis. The instruments at the LE site are calibrated every two years using class A pyranometers and pyrheliometers (Kipp & Zonen CMP22 and CHP1, respectively, kept in storage) with traceability to the World Radiometric Reference (WRR) at World Radiation Center (WRC) in Davos, Switzerland. At the LU site, instruments are periodically compared to a calibrated Kendall absolute cavity radiometer, also with WRR traceability, which is kept in storage and used sporadically as a reference. As mentioned, the SM site is part of the Brazilian SONDA network, installed and managed by the Instituto Nacional de Pesquisas Espaciais (INPE) (Dias da Silva et al., 2014).

Site	Site code	Lat.(°)	Lon.(°)	Alt. (m)	Data period
LES (Salto)	LE	-31.28	-57.92	56	01/2015–12/2017
São Martinho da Serra	MS	-29.44	-53.82	489	01/2010–12/2016
Luján	LU	-34.59	-59.06	30	01/2010–12/2012

Table 2: Measurement's sites information. The columns show the site's code, the spatial coordinates and altitude above sea level, and the period span of the measurements used in this work.

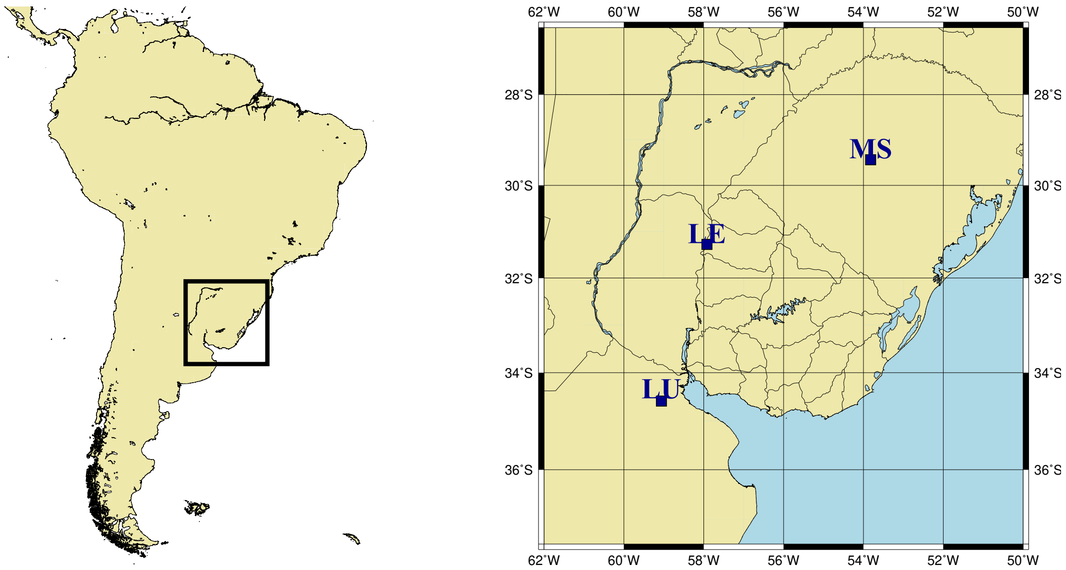

(a) Region of study.

(b) Measurement site locations.

Figure 1: Site locations to test the proposed DNI satellite-based CIM models in this work.

Quality control

The set of measurements includes pairs of simultaneous (GHI, DNI) values registered at the 1-minute level as a result of an average of 6 instantaneous values taken at 10-second intervals. Then, measurements are integrated into hourly values (in $\mathrm{Wh/m^2}$) as long as at least 2/3 of the one-minute data are available for each hour. The hourly data series of DNI and GHI are subjected to a basic quality control procedure based on a visual inspection and four successive filters described schematically in Table 3.

The first three filters are conceptually similar and consist of upper bounds for the irradiation values. The first criterion is the BSRN recommendation to filter extremely rare values (Long and Shi, 2008). The second one is to impose an upper envelope for each component determined by the ESRA clear sky model (Rigollier et al., 2000) with an artificially low turbidity value for the specific region ($T_L = 1.8$, in this case). The third one consists of a threshold for the modified clearness index Perez et al. (1990) for GHI, and the determination of a typical region of the data on the (k_t, k_n) space, where k_t is the usual clearness index (ratio between GHI and its corresponding irradiation at the top of the atmosphere, TOA) and k_n is the broadband direct transmittance (ratio between DNI and TOA irradiation at normal incidence). The measurements outside this region are discarded as problematic. An example is shown in Figure 2, for the LE site. This last criterion is capable of removing misalignment errors and other problematic data. The SERI-QC procedure (Maxwell et al., 1993) bounds this typical region by two characteristic double exponential curves (also known as Gompertz curves), which are empirically and visually adjusted for each site. Finally, the fourth filter removes the measurements with solar altitudes lower than 7°, which, in the case of GHI, are affected by the cosine error.

Filter	Component	Condition	Description
i	**GHI**	$-2\ \text{Wh/m}^2 < I_h < I_0\, 1.2\, \cos\theta_z^{1.2} + 50\ \text{Wh/m}^2$	BSRN extremely rare
	DNI	$-2\ \text{Wh/m}^2 < I_b < I_0\, 0.75\, \cos\theta_z^{1.2} + 30\ \text{Wh/m}^2$	limits (Long and Shi, 2008).
ii	**GHI**	$0\ \text{Wh/m}^2 < I_h < I_h^{ESRA}$	ESRA clear sky model upper
	DNI	$0\ \text{Wh/m}^2 < I_b < I_b^{ESRA}$	limit ($T_L = 1.8$).
iii	**GHI**	$k_{tp} < 0.85$	Modified clearness index threshold.
	GHI & DNI	Typical region of $(k_t,\ k_n)$ space	Based on SERI-QC
		determined by Gompertz curves.	(Maxwell et al., 1993).
iv	**GHI & DNI**	$\alpha_s > 7°$	Minimum solar altitude.

Table 3: Quality control filters applied on GHI and DNI irradiation components. The TOA irradiation is denoted by I_0, and the supra-index ESRA denotes that the corresponding variable is estimated with this clear sky model.

The Table 4 shows the results of the quality control procedure for each site. On average, 85% of the data meets the quality criteria for its use in this work. After the quality procedure, 25517 hours of DNI records are used.

	Diurnal data	**Filter (ii)**		**Filter (iii)**		**Filter (iv)**		
site	**valid data**	**disc.**	**hours**	**disc.**	**hours**	**disc.**	**hours**	**selected**
LE	9474	0.0%	9473	13.8%	8168	5.0%	**7758**	**81.9%**
MS	15390	0.0%	15387	9.8%	13876	4.1%	**13303**	**86.4%**
LU	5262	0.5%	5235	11.3%	4644	4.0%	**4456**	**85.1%**
total	**30126**	**0.2%**	**30095**	**11.3%**	**26688**	**4.4%**	**25517**	**84.7%**

Table 4: Results of the quality control of hourly DNI measurements. The starting set is the valid data selected after passing filter (i) and a visual inspection. The percentage of samples discarded by each criterion is shown. The last two columns show the number of samples that passed all filters and its percentage of the initial set.

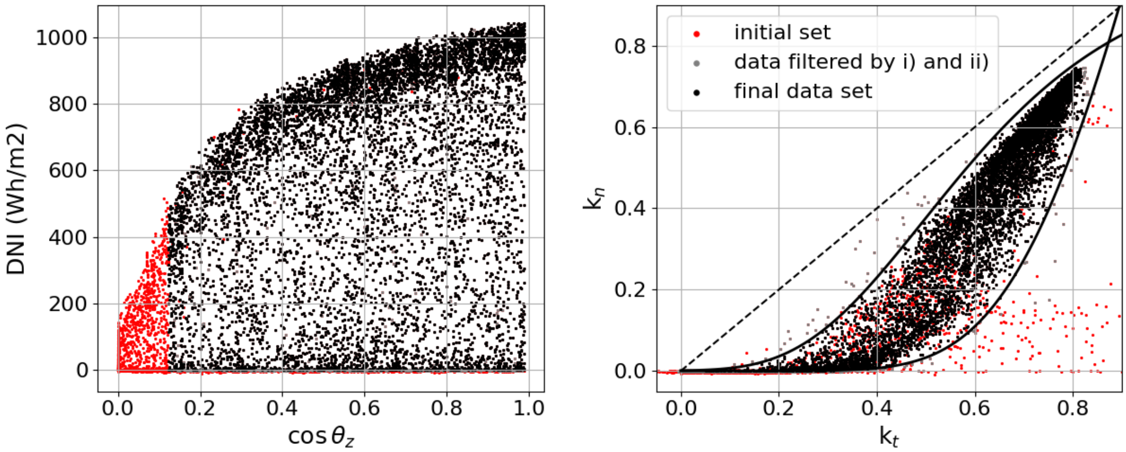

(a) DNI vs cosine of the solar zenith angle.

(b) Quality filters in the k_t–k_n space.

Figure 2: Quality filtering results for the LE site showed in two diagrams. In the right plot, the lines show the double exponential boundaries (Gompertz functions) used to determine a typical region for each site's data. The $x = y$ is also included (dashed line) as reference.

2.2. GOES-East satellite visible channel images

As mentioned in the introduction, CIM models quantify the effect of cloudiness in the ground-level solar irradiance by using satellite information in the visible range. Cloudiness can be challenging to distinguish from the background in areas with a high albedo, such as snow-covered, desert, or salt flats. In these cases, including more cloud information from GOES infrared images, atmospheric modeled data, or other satellites becomes necessary. The target region of this study does not include such areas, making additional satellite information unnecessary. By this, the model's scope is limited to moderate or low albedo sites. However, its ease of use and minimal input requirements compensates, as can be applied widely and easily without compromising its performance. Incorporating more cloud information is critical to extending the model's applicability to all-site coverage.

The satellite images used in this work are from the GOES-East geostationary satellite (placed above the 75°W meridian), which has a viewing angle of approximately 40° over the region of interest (Laguarda et al., 2020). The GOES-13 physical satellite was operational during the considered period[3] at that location and its visible range (wavelengths between 0.54 µm and 0.71 µm) images were considered in terms of Reflectance Factor, F_R. Under normal operating conditions, the GOES-13 satellite generated two images per hour for South America. However, this operational regime could be affected to monitor closely meteorological priorities like hurricane events in the Caribbean and USA's East and Central coasts, leaving South America occasionally with images every 3 hours only. Hourly reflectance factor series, F_R, were obtained for this

[3]GOES13 was operative from April 2010 to December 2017.

work for the three sites with ground data and for the period of interest via linear interpolation of the Earth's albedo $\rho = F_R/\cos\theta_z$, being θ_z the solar zenith angle.

There is a compromise between using instantaneous satellite images[4] to represent an hourly average over a site. This issue is solved here via an ergodic assumption, using a spatial average in small cells containing each site. The spatial average of an instantaneous image represents better the mean irradiance behavior within the hour. This idea has been successfully applied to GHI satellite estimation (Laguarda et al., 2020), improving CIM performance. For this work we use as cell area a latitude-longitude rectangle of 15×18 km, and perform the same spatial average as in Laguarda et al..

2.3. Atmospheric information from MERRA-2

The CIM models require accurate estimates of DNI under clear sky conditions. Clear sky models rely on quality atmospheric information for its accuracy. In this work, we consider two clear sky models, detailed in Subsection 3.1, with different atmospheric information as inputs. One of these sources is the NASA's Modern-Era Retrospective Analysis for Research and Applications database version 2 (MERRA2, Gelaro et al. (2017)). MERRA2 is a reanalysis data set obtained from the Global Earth Observing System Version 5 (GEOS-5) atmospheric model. It provides hourly averages for several atmospheric variables over the entire globe, for the period 1980 to present, with spatial resolution of $0.5° \times 0.625°$. MERRA2 integrates measurements from different sources, such as the Aqua and Terra MODIS instruments, the MISR (Multiangle Imaging SpectroRadiometer), the AVHRR (Advanced Very-High-Resolution Radiometer) for 2000-2014 and airborne sensors (1980-2002). It also incorporates ground-based observations from the Aeronet network (https://aeronet.gsfc.nasa.gov/).

In Gueymard and Yang (2020), MERRA2 estimates for aerosol-related variables such as Aerosol Optical Depth at 550 nm (AOD_{550}) and the Angström exponent (α) are evaluated over different climatic regions (characterized by their Köpen-Geiger classification) over the 2003-2017 period, using ground measurements from 800 Aeronet sites as a reference. For a Cfa climate (as the target region in this work), AOD_{550} shows a mean bias (rMBD) of -1.1% and a rRMSD of 35%, averaged over the three Aeronet sites in the region (Córdoba, CEILAP Buenos Aires and São Martinho da Serra). In a local study, Laguarda and Abal (2020) evaluated the accuracy of MERRA2 estimates for AOD_{550}, Angström's exponent α and precipitable water vapor over the same three Aeronet sites obtaining an rRMSD of 33.4% for AOD_{550}, 26.8% for α and 11.2% for water vapor. It is clear that MERRA2 provides a rather high uncertainty when estimating aerosol-related variables, as evidenced by the AOD_{550} estimation, which has rRMSD above 30% in both studies. Although this limitation, the benefit of accessing a cohesive archive of atmospheric data from around the world through a single source is significant.

[4] Indeed, the geostationary satellite images are quasi-instantaneous, as the radiometer detector's array scans each pixel at different moments. The time difference between pixels' scans is of some minutes and a correction on this is not usually applied.

3. Proposed DNI model (LCIM)

The proposed DNI model, named LCIM (**L**ES **C**loud **I**ndex **M**odel), follows the basic structure of all CIM models,

$$\hat{I}_b = I_b^{cs} \times F(\eta), \tag{1}$$

where $\hat{I}_b$ is the model's DNI estimate, I_b^{cs} is a clear sky DNI estimate and F is a cloud modifier factor expressed as a function of the satellite cloud index, η, defined next in Subsection 3.2. The success of a CIM model depends on the accuracy of the clear sky model, as well as on the definition of the cloudiness index η and the empirical determination of its relationship with the attenuation factor, F.

3.1. Clear sky models

In order to determine the best option to estimate clear sky beam irradiation, we considered several clear sky models with different characteristics. For brevity, here we present results for the two with the best performance over the region:, REST-2 (Gueymard, 2008) and McClear (Lefèvre et al., 2013). The first is operationally implemented while the second provides downloadable online estimates for arbitrary sites over the globe. These clear sky models have been previously assessed and highlighted among other alternatives due to their performance (Gueymard, 2012; Engerer and Mills, 2015; Ineichen, 2016; Ruiz-Arias and Gueymard, 2018; Antonanzas-Torres et al., 2019). The clear sky samples required for the present model's evaluation were selected from the filtered hourly data set by extensive visual inspection aided by the calculation of common quantities as the hourly and daily clearness indexes (k_t, and also k_{tp} at hourly level) and the direct transmittance (k_n).

REST2 estimates DNI and other irradiance components (Gueymard, 2008). It is related to the SMARTS2 spectral model (Gueymard, 2018) but in two sub-bands: 290–700 nm (ultraviolet and visible) and 700–4000 nm (near infrared). The model uses up to 8 atmospheric variables as input, being the most relevant the aerosol-related quantities, Angstöm turbidity factor (β) and exponent (α), and the precipitable water column, available from the MERRA-2 database described in Subsection 2.3. With this input information, REST2 clear sky DNI estimates have a rRMSD of 6.4% and a rMBD of -2.8% over the three SESA sites, as reported in Table 5. The McClear clear sky model is based on LibRadTran Radiative Transfer calculations (Mayer and Kylling, 2005) and works operationally as a look-up table (Lefèvre et al., 2013). For estimating GHI, DHI and DNI, information of aerosol content, precipitable water and ozone columns and surface albedo are required. This atmospheric information is provided at three-hour intervals by the Copernicus Atmosphere Monitoring Service (CAMS) reanalysis database, while the daily albedo is obtained from NASA's MODIS imagery, https://modis.gsfc.nasa.gov/data/dataprod/. McClear's hourly estimates are publicly available at the CAMS website (https://atmosphere.copernicus.eu/) with global coverage. The original resolution is 50-150 km and the download procedure includes an interpolation that generates estimates at any location with time resolution up to 1 minute. The McClear model estimates DNI in the SESA region with rRMSD of 6.3% and rMBD of −1.1%.

model	**atmospheric info.**	**rMBD** (%)	**rRMSD** (%)	**KSI** (Wh/m^2)
REST2	MERRA2	-2.8	6.4	26.3
McClear	CAMS	-1.1	6.3	21.2

Table 5: Performance of the clear sky models as implemented in this work. Performance indicators are expressed as a percentage of the mean hourly clear sky DNI ($I_b = 836\,\mathrm{Wh/m^2}$). The evaluation is based on 2493 clear sky samples (831 values per site, on average). KSI is the Kolmogorv-Smirnoff Index, measuring the absolute difference between the cumulative distributions functions of the estimated and measured DNI.

As summarized in Table 5, both clear sky models have a similar performance over the target area (see rRMSD and KSI), with McClear showing a smaller bias. However, both have different characteristics and, in our implementation, are based on different atmospheric data sets.

3.2. Cloud attenuation

To quantify the pixels' cloudiness from visible channel images, the planetary (or Earth) albedo (ρ) is calculated by normalization with a dynamic range of extreme values (minimum and maximum) obtaining a cloud index η bounded by unity and zero (Cano et al., 1986),

$$\eta = \frac{\rho - \rho_{min}}{\rho_{max} - \rho_{min}} \qquad \text{for} \qquad \rho_{min} < \rho < \rho_{max}. \tag{2}$$

The minimum values, associated with clear skies, present seasonal and intra-day variations that depend on each pixel, i.e. ρ_{min} is a time-varying map over the area of interest. On the other hand, the maximum values are associated with overcast skies and have no evident seasonal dependence. To ensure that η is in the range [0,1], the constrains $\eta = 1$ for $\rho > \rho_{max}$ and $\eta = 0$ for $\rho < \rho_{min}$ are imposed. To estimate the intra-day and seasonal variation of the background albedo ρ_{min}, the parametrization proposed in Tarpley (1979) and adapted to GOES-East reflectance factor in Alonso-Suárez (2017) is adjusted for each pixel in the image using the satellite clear sky samples, which are automatically selected from the pixel's satellite time-series by a robust iterative procedure, described in detail in Alonso-Suárez et al. (2012).

The maximum value ρ_{max} is related to the saturation of ρ under overcast skies. In this proposal this is determined by an empirical constant. Its value for DNI estimation is adjusted to local conditions by using the ground measurements, showing an optimum value (in terms of RMSD) of $\rho_{max} \simeq$ 0.46-0.54, as shown in Figure 3. This figure illustrates the rRMSD variation of each LCIM model with respect to ρ_{max}, using the same LCIM structure and different clear sky estimates. The bands in transparency shown one standard deviation between the three measuring sites. This value of ρ_{max} is in agreement with the one reported by Ceballos et al. (2004) for satellite DNI estimation ($\rho_{max} = 0.465$). This exact value was found statistically by Ceballos et al. from the satellite images by seeking to identify the reflectance's threshold value between cumuliform and stratiform clouds in overcast skies, for which the DNI attenuation regime changes significantly.

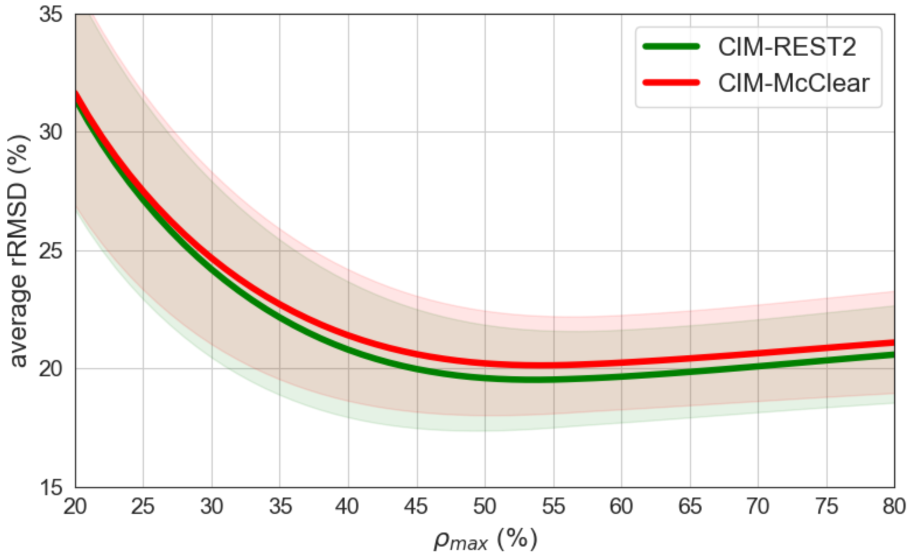

Figure 3: rRMSD of the optimized LCIM using ρ_{max} as a parameter. Each line corresponds to a different clear sky model and the transparency bands represent the standard deviation over the three sites. The minima are shallow and, for simplicity, this parameter is fixed at $\rho_{max} = 0.5$ (or 50%) for all models.

According to Eq. (1), the cloudiness factor, F, represents a clear sky index for the direct irradiation, $k_{b,cs} = I_b/I_b^{cs}$. Figure 4 shows the dependence of this ratio with $(1 - \eta)$ for the LE site, using the REST2 clear sky model as basis for the $k_{b,cs}$ calculation and DNI measurements. A dependence on the solar zenith angle (mapped in the color of the points) is not evident. In change, a clear dependence between the two plotted variables is observed. In Laguarda et al. (2020) we noted that for GHI, the relationship of k_c (GHI clear sky index) and $(1-\eta)$ can be modeled as linear, which is also used in other satellite GHI models (Perez et al., 2002). In this case, it is evident that a more complex relationship is required for DNI. In order to maintain only two adjustable parameters (a and b), a quadratic dependence is proposed,

$$F(\eta) = a\,(1 - \eta)^2 + b. \tag{3}$$

It is expected that DNI suffers low attenuation with respect to the clear sky estimate when there are no clouds ($\eta \simeq 0$) and total attenuation under overcast skies ($\eta = 1$). By having integrated data in one hour, the average behavior results and the effects of partial cloudiness are softened. That is why Eq. (1) shows an accumulation of points with $k_{b,cs}$ less than 0.1 and a smooth transition (associated with partial cloudiness) towards values close to 1. Due to all these, the quadratic adjustment is carried out keeping both parameters (a and b) independent, and b is expected to be close to zero.

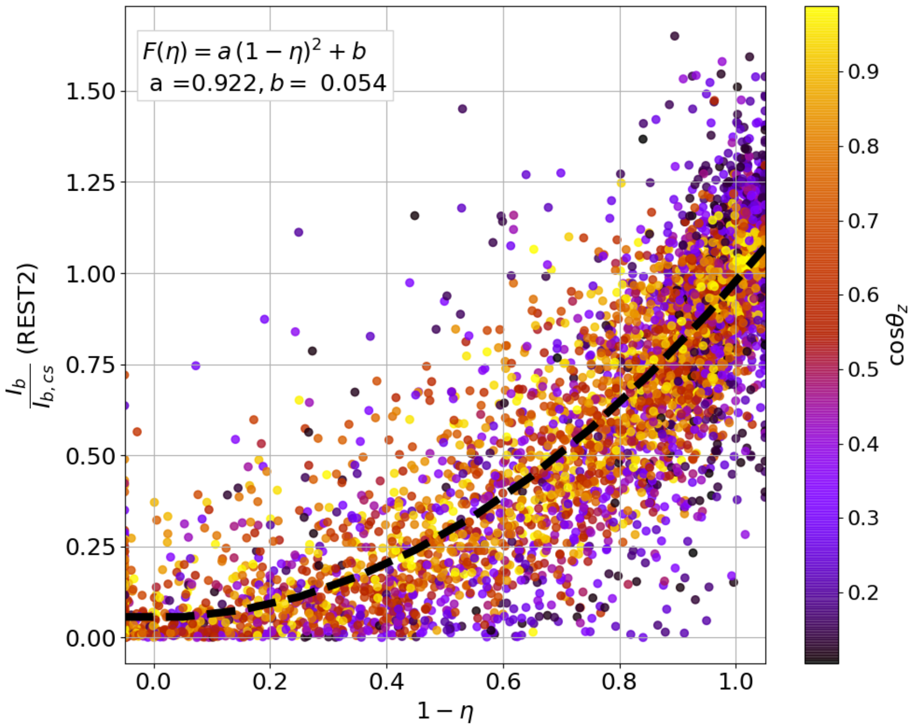

Figure 4: Behaviour of the beam clear sky index using REST2 model at LE site.

Table 6 shows, for each site, the cloudiness factor parameters a and b. The adjustment of these coefficients is done along with the performance assessment (shown in Section 4) using a standard cross-validation procedure in which the data set is divided into two separated halves that are used for training and validation, respectively. This procedure is repeated 1000 times with random sampling to ensure repeatability, and the average coefficients' value and performance metrics are reported. The last column shows the spatial average and the relative inter-site standard deviation of the mean (in parentheses), showing that the results are consistent over the three sites for each model. The inter-model average value of a is 0.89 and shows low spatial variability in all cases, while the independent term, b, is on average 0.055 with greater relative variations, depending on the model and site. In Laguarda et al. (2020), in the context of CIM models for GHI, the spatial robustness of the parameters allowed the application of a single average value of each coefficient at arbitrary locations in the region, without significant loss of precision. The same observation can be made for the DNI models presented here.

4. All-sky DNI model performance

The basic performance metrics for the two CIM variants for DNI estimation are shown in Table 7. The last row shows the mean measured DNI used for metrics' normalization at each site and the last column

Model	Parameter	LE	MS	LU	Average
CIM-McClear	**a**	0.875	0.836	0.901	**0.882 (3.8%)**
	b	0.061	0.061	0.052	**0.057 (8.6%)**
CIM-REST2	**a**	0.922	0.859	0.899	**0.905 (3.6%)**
	b	0.054	0.063	0.045	**0.051 (16.7%)**

Table 6: Cloud factor coefficients, Eq. (3), for each DNI CIM model using different clear sky estimates. The last column shows the average across sites with its site dispersion in parenthesis.

shows the average for all sites. This is a weighted average in which the estimated relative uncertainty associated with each data series is taken into account. By considering the maintenance schedule of each station, a relative uncertainty of 2% was assigned to the LE and LU sites and 4% to the MS site. The normalized squared inverse of these uncertainties was used as weights for the average, thus giving more importance in this model's assessment to the lower uncertainty data records. Small biases (less than $\pm 0.7\%$) are obtained for both models at all sites. Low biases are to be expected, since the coefficients a and b play the role of a local adjustment. The averaged dispersion (quantified by the rRMSD) is between 18.4 and 19.1% and the KSI is between 15.8 and 18.4 Wh/m^2. These metrics suggest that the CIM-REST2 with MERRA2 inputs has greater accuracy than CIM-McClear with CAMS atmospheric information, for which a small systematic underestimation persists in all three sites.

Model	Metric	LE	MS	LU	Average
CIM-REST2	rMBD (%)	-0.2	$+0.1$	0.0	**$-$0.1 (0.2)**
	rRMSD (%)	17.1	22.4	18.7	**18.4 (2.7)**
	KSI(Wh/m^2)	14.0	18.6	16.8	**15.8 (2.3)**
CIM-McClear	rMBD (%)	-0.4	-0.1	-0.7	**$-$0.5 (0.3)**
	rRMSD (%)	17.4	22.8	19.8	**19.1 (2.7)**
	KSI(Wh/m^2)	15.5	19.4	21.0	**18.4 (2.8)**
	# data points	7622	12956	4376	**24934**
	$\langle I_b \rangle$(Wh/m^2)	579.3	472.4	548.0	**553 (55)**

Table 7: Performance of DNI estimates for CIM with different clear sky models. The last rows show the number of data pairs used (considering quality measurements and satellite availability) and the irradiation average over sites.

Figures 5a and 5b show the scatter plots comparing the DNI estimates from each model to the corresponding ground measurements. The density of points is mapped to a green-yellow color map. The two high-density regions correspond to clear sky (high DNI) and overcast skies (low DNI). This can also be observed in the bimodal probability density plots shown in Figure 5c. Under clear sky conditions, the scatter plots for both CIM models do not exhibit any apparent bias. However, the density plot indicated that the CIM-REST2 model is a closer approximation to the clear sky data probability distribution. The dispersion is larger at intermediate values of DNI, indicating that DNI CIM methods have difficulties in accurately modeling irradiation under partial cloudiness conditions. It can also be noticed that the CIM-ESRA model has more difficulties in capturing the probability distribution of the DNI-measured data. Both CIM models are imprecise in representing the lower DNI values' probabilities, indicating room for improvement in predicting values close to zero. The CIM-REST2 is the best overall model from the probabilities point of view, correspondingly coinciding with the lowest metrics (and the KSI value in particular).

Contextualization with alternative approaches for DNI estimation

A first contextualization of the previous results arises from the comparison with DNI satellite-based estimations for other regions, such as those described in Table 1, keeping in mind that models can not be ranked nor compared using data from different locations or even different periods for the same location. Direct comparison is hindered by another issue, which is the lack of information in most previous studies about satellite spatial averaging and its ability to account for hourly values in an ergodic manner. The hourly performance can be enhanced by this factor. The only study that discusses ergodicity is the one conducted by Porfirio and Ceballos (2017), which used a cell size of approximately 12×12 km. However, the evaluation was performed on a daily time scale, making the comparison unfeasible. The results presented in Table 7 must be framed in this context, in particular, concerning the known performance of the other satellite-based DNI models at other locations.

Another approach for DNI estimation is to use GHI information (either from measurements or from a satellite-based model) and a phenomenological diffuse fraction model estimate the diffuse component. Then

$$\mathrm{DNI} = \mathrm{GHI} \times \frac{1 - f_d}{\cos\theta_z}. \tag{4}$$

where f_d =DHI/GHI is the diffuse fraction. Since the separation problem depends on the typical local atmospheric composition there are many phenomenological models in use looking for the best balance between a minimal set of predictors and acceptable accuracy (Gueymard and Ruiz-Arias, 2016). Abal et al. (2017) locally adjusted and evaluated ten separation models using data from the same target region of this work. Of these, the one by Ruiz-Arias et al. (2010) strikes the best balance between simplicity of use and performance, being also operational (i.e. it does not require future information as input). This model (referred to as RA2s, according to the nomenclature of Abal et al.) has the form of a double exponential function,

$$f_d = a_0 - a_1\, e^{-\exp(a_2 + a_3 k_t + a_5 m)}, \tag{5}$$

with the set of locally adjusted parameters (a_i for $i = 0 \ldots 5$), for the specific values valid for the whole region see Abal et al. (2017). The RA2s model is then essentially unbiased and can estimate the diffuse

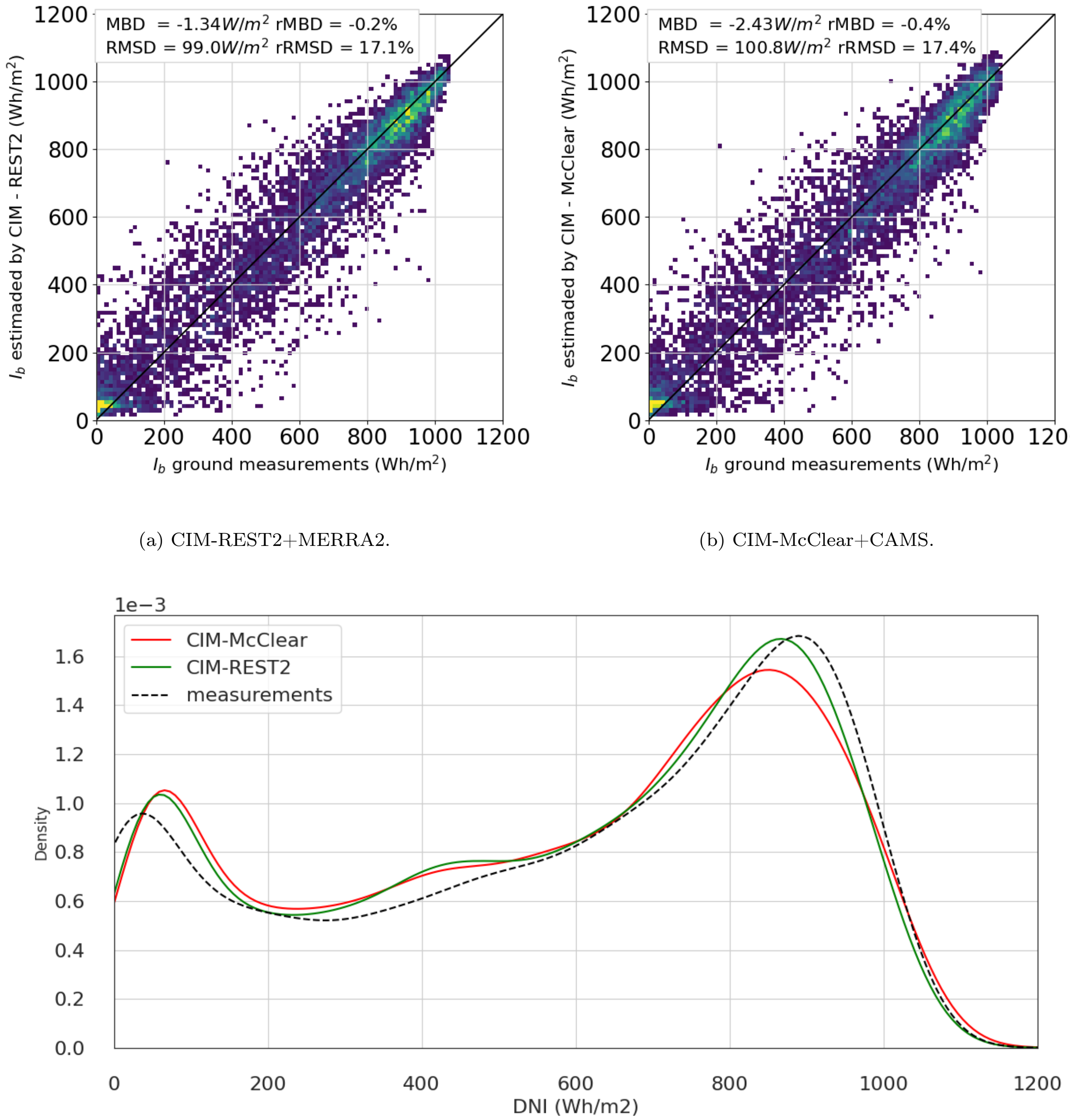

(a) CIM-REST2+MERRA2.

(b) CIM-McClear+CAMS.

(c) Probability density plot.

Figure 5: Scatter plots for each model in the LE site (a and b subplots). The density of points is mapped to green-yellow colors. The last panel (c) shows the density plots for both models and the measurements (dashed line).

fraction with an rRMSD under 20%, relative to an average value $< f_d >= 0.47$.

An obvious problem with this approach is that the error in the DNI estimates increases for low-Sun altitudes due to $\cos\theta_z = \sin\alpha_s$ becoming very small. The expression is also affected by the high uncertainty of empirical diffuse fraction models, which do not attempt to model in detail the complex scattering processes in the atmosphere. This becomes particularly relevant under partly cloudy sky conditions. However, due to its convenience, this phenomenological approach is still used in practice to estimate DNI in the absence of more reliable information. Table 8 shows the performance indicators when estimating DNI from either GHI measurements or GHI satellite estimates, by using Eqs. (4) and (5). This analysis has been done with the same data set used in Table 7 and is intended to provide a comparison of this simplified approach with the direct satellite DNI estimation from CIM models. For the case in which GHI satellite estimates are used, a satellite model needs to be selected. In (Laguarda et al., 2020), two CIM models for GHI, based on the ESRA (Rigollier et al., 2000) and McClear clear sky models, were implemented and evaluated with very good results for ten sites in the same region of this work (including the three sites used here). The simple CIM-ESRA model was unbiased and achieved an hourly rRMSD of 12.5% (based on an average GHI of 448 $\mathrm{Wh/m^2}$), which was found comparable to more complex models[5]. These GHI estimates are used in Table 8. DNI estimated from both indirect models shows significant positive biases for all sites ($\simeq$ 6-7% on average). This is due to the use of the RA2s diffuse fraction model under partially cloudy skies, as was previously observed for data from the same region Abal et al. (2017). This causes an overestimation of DNI, after Eq. (4). This overestimation can be seen in the scatter plots of Figure 6 (LE site), particularly under partly cloudy conditions. The DNI estimated from ground measurements has a rRMSD of $\simeq$ 17% which increases to $\simeq$ 25% when satellite-based GHI is used, showing that the use of GHI satellite estimates in this indirect procedure significantly degrades the accuracy of the DNI estimation. This means that when GHI ground measurements and a locally adjusted diffuse fraction model are available, the simplified procedure yields acceptable performance compared to satellite-based DNI models. The requirement of a local diffuse fraction model presupposes that diffuse horizontal irradiance measurements are available at the site or in the surrounding area, which is not usually the case. In addition, the competitive ground-based strategy requires on-site GHI measurements. When the standalone satellite estimation is considered, it is clear that a dedicated satellite-based DNI model should be the preferred strategy, as all metrics are significantly better.

These results indicate that CIM based satellite-based estimation of DNI is more accurate than indirect approaches based on phenomenological separation models, so it should be preferred for low to moderate albedo regions if satellite information is available. Other phenomenological direct-diffuse separation models may be considered, but we do not expect at hourly level a different conceptual conclusion in this target region.

[5]The CIM-McClear for GHI performed slightly better (Laguarda et al., 2020) and the CIM-REST2 for GHI with MERRA2 atmospheric information gives very good estimates also (Laguarda, 2021). Since for GHI estimation all these CIM models have similar performances for this region at the hourly level, any of them can be used equivalently.

Site	**LE**	**MS**	**LU**	**Average**
Model	GHI from measurements and Eq. (5)			
rMBD (%)	+4.3	+9.6	+9.3	**+7.1**
rRMSD (%)	14.4	19.1	18.3	**16.7**
KSI (Wh/m^2)	35.0	46.1	51.7	**43.7**
Model	GHI from CIM-ESRA and Eq. (5)			
rMBD (%)	+3.2	+8.5	+8.3	**+6.1**
rRMSD (%)	22.9	29.2	25.9	**24.9**
KSI (Wh/m^2)	59.0	57.9	65.6	**61.8**

Table 8: Performance indicators for the two indirect methods to estimate DNI from Eq. (4) and the RA2s separation model.

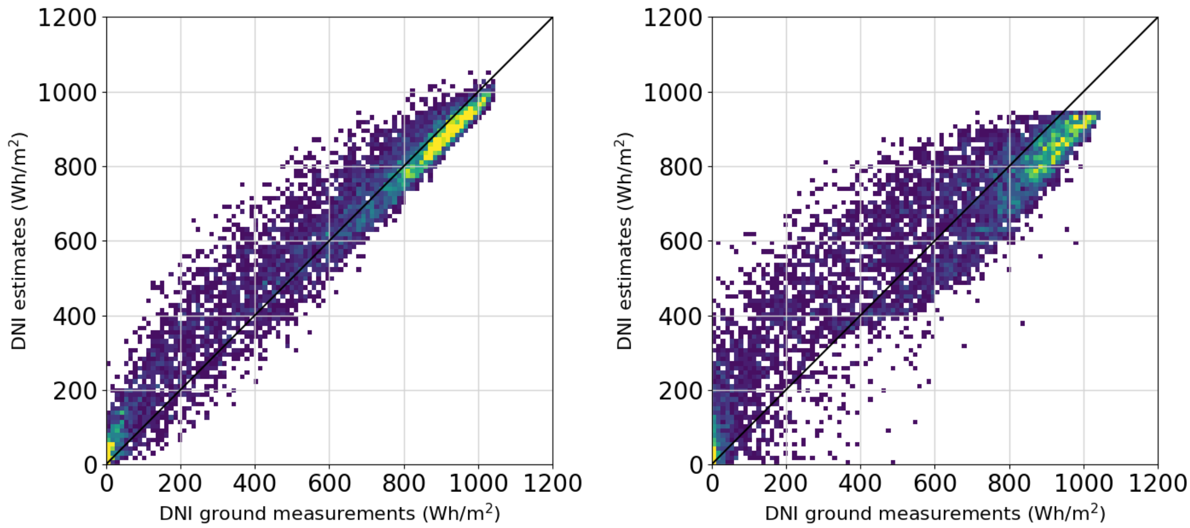

(a) DNI estimated from measured GHI.

(b) DNI estimated from GHI satellite estimates (CIM-ESRA).

Figure 6: Scatter plots for the DNI at the LE site obtained by indirect methods based on the RA2s phenomenological direct-diffuse separation model locally adjusted for the region.

The situation may be different in other regions with different climates or typical geographical conditions.

5. Conclusions

Two new variants of a Cloud Index Model (CIM) that directly estimate hourly DNI are proposed, implemented and assessed. These models achieve typical uncertainties of less than 20% when evaluated with data from three sites in the Southeastern South America region (SESA) region. This area has a moderate surface albedo and is known to exhibit challenging intermediate short-term solar irradiance variability. This article extends to DNI estimation the findings of Laguarda et al. (2020) for the (simpler) case of satellite-based GHI estimation.

The key elements introduced in this article are (i) a simple quadratic dependence of the attenuation factor (F) on the cloud index and (ii) an ad-hoc procedure to calculate the satellite-based cloud index η for the DNI case. Two CIM variants are considered, based on different clear sky models (REST2 and McClear) and different sources for the required atmospheric information. REST2 is implemented with hourly atmospheric information from the MERRA2 reanalysis database and McClear uses atmospheric information from the Copernicus Atmospheric Monitoring Ssystem (CAMS, available every three hours). The CIMs are locally adjusted by tuning two attenuation factor coefficients using local DNI measurements. As a result, the CIM-DNI models are essentially unbiased (with average bias deviations within $\pm 0.5\%$). The typical dispersion obtained, averaged over sites, was below 20% (in terms of rRMSD) for both variants. In the context of satellite-based DNI estimation worldwide, this can be considered a good indicator, even for locally adjusted models. The proposed quadratic relation between F and η is required, as opposed to CIM models for GHI estimation, for which a linear relation is good enough. The two adjusted parameters have low spatial variability across the three sites, suggesting they can be used in the broad SESA region without significant degradation of performance. In fact, the determination of the cloud factor F from satellite information is the most delicate aspect of the proposed CIM models' implementation but it must be done once, since the results are applicable over large homogeneous geographical regions.

These good results are achieved at a low cost in terms of implementation. The variant CIM-McClear does not even require the user to implement a clear sky model or deal with atmospheric data, since McClear's estimates are downloaded from the CAMS website for arbitrary locations. The other variant is based on a clear sky model that can be locally implemented without difficulty and on atmospheric data which can be accessed from the publicly available MERRA2 site.

An alternative method based on the use of phenomenological diffuse-direct separation models to obtain DNI from GHI estimated from a satellite CIM was tested. The results indicate a significant bias between 3 and 8% and a rRMSD between 23 and 30%, depending on the site. The CIM-DNI models presented here represent the best alternatives for DNI estimation in this region. Both have similar performance and, depending on the application, one or the other strategy may be used. For research purposes, CIM-REST2 with MERRA-2 atmospheric information is relatively simple to implement and provides full control over the generated estimates. The CIM-McClear DNI estimates are delivered operationally, making it convenient for some technological applications. Its use implies a lack of control, as the McClear model is not easy to implement locally due to its inherent complexity.

As stated, even if the results presented in this article are specific to the SESA geographical region, which has only moderate ground albedos, similar ideas can be applied successfully in other regions, provided they do not have areas with high albedos (typically associated with deserts, permanent snow cover or salt flats). Some of these regions exist in South America, so in future work these CIM models should be extended by using infrared channel satellite information in order to successfully distinguish clouds in images with high surface albedos. This could result in greater generality, provided an acceptable performance is obtained over a continental scale.

Acknowledgments

The authors thank the teams responsible for the ground data collection at the BSRN site of São Martinho da Serra, Brazil, and at the GERSOLAR laboratory of the Universidad Nacional de Luján, Argentina. The authors acknowledge financial support by the CSIC I+D Group's program of Udelar, Uruguay.

References

Abal, G., Aicardi, D., Suárez, R. A., and Laguarda, A. (2017). Performance of empirical models for diffuse fraction in uruguay. *Solar Energy*, 141:166–181.

Alonso-Suárez, R. (2017). *Estimación del recurso solar en Uruguay mediante imágenes satelitales*. PhD thesis, Facultad de Ingeniería, Universidad de la República. Tesis de Doctorado en Ingeniería.

Alonso-Suárez, R., Abal, G., Siri, R., and Musé, P. (2012). Brightness-dependent Tarpley model for global solar radiation estimation using GOES satellite images: application to Uruguay. *Solar Energy*, 86(11):3205–3215.

Alonso-Suárez, R., David, M., Branco, V., and Lauret, P. (2020). Intra-day solar probabilistic forecasts including local short-term variability and satellite information. *Renewable Energy*, 158:554–573.

Antonanzas-Torres, F., Urraca, R., Polo, J., Perpiñán Lamigueiro, O., and Escobar, R. (2019). Clear sky solar irradiance models: A review of seventy models. *Solar Energy*, Renewable and Sustainable Energy Reviews:374–387.

Beck, H., Zimmermann, E., McVicar, T., Vergopolan, N., Berg, A., and Wood, E. (2018). Data descriptor: Present and future köppen-geiger climate classification maps at 1-km resolution. *Scientific Data*, 5:180214:1–12.

Bettolli, M. L., Solman, S. A., da Rocha, R. P., Llopart, M., Gutierrez, J. M., Fernández, J., Olmo, M. E., Lavin-Gullon, A., Chou, S. C., Rodrigues, D. C., Coppola, E., Balmaceda Huarte, R., Barreiro, M., Blázquez, J., Doyle, M., Feijoó, M., Huth, R., Machado, L., and Cuadra, S. V. (2021). The CORDEX Flagship Pilot Study in southeastern South America: a comparative study of statistical and dynamical downscaling models in simulating daily extreme precipitation events. *Climate Dynamics*, 56:1589–1608.

Cano, D., Monget, J., Albuisson, M., Guillard, H., Regas, N., and Wald, L. (1986). A method for the determination of the global solar radiation from meteorological satellite data. *Solar Energy*, 37:31–39.

Ceballos, J. C., Bottino, M., and de Souza, J. (2004). A simplified physical model for assessing solar radiation over Brazil using GOES 8 visible imagery. *Journal of Geophysical Research: Atmospheres*, 109(D2).

Dias da Silva, P. E., Martins, F. R., and Pereira, E. B. (2014). Quality control of solar radiation data within SONDA network in Brazil: preliminary results. In *ISES Conference Proceedings, EuroSun 2014*, Solar Radiation Availability and Variability, pages 1–9.

Djebbar, R., Morris, R., Thevenard, D., Perez, R., and Schlemmer, J. (2012). Assessment of suny version 3 global horizontal and direct normal solar irradiance in canada. *Energy Procedia*, 30:1274–1283. 1st International Conference on Solar Heating and Coolingfor Buildings and Industry (SHC 2012).

Engerer, N. and Mills, F. (2015). Validating nine clear sky radiation models in Australia. *Solar Energy*, 120:9–24.

Gelaro, R., McCarty, W., Suârez, M., Todling, R., Molod, A., Takacs, L., Randles, C., Darmenov, A., Bosilovich, M., Reichle, R., and Wargan, K. (2017). The modern-era retrospectiveanalysis for research and applications, version 2 (merra-2). *Journal of Climate*, 30:5419–5454.

Gueymard, C. (2018). Smarts code, version 2.9.8 user's manual. Technical report, Solar Consulting Services.

Gueymard, C. and Ruiz-Arias, J. (2016). Extensive worldwide validation and climate sensitivity analysis of direct irradiance predictions from 1-min global irradiance. *Solar Energy*, 128:1–30. Special issue: Progress in Solar Energy.

Gueymard, C. and Yang, D. (2020). Worldwide validation of CAMS and MERRA-2 reanalysis aerosol optical depth products using 15 years of AERONET observations. *Atmospheric Enviroment*.

Gueymard, C. A. (2008). Rest2: High-performance solar radiation model for cloudless-sky irradiance, illuminance, and photosynthetically active radiation – validation with a benchmark dataset. *Solar Energy*, 82(3):272–285.

Gueymard, C. A. (2012). Clear-sky irradiance predictions for solar resource mapping and large-scale applications: Improved validation methodology and detailed performance analysis of 18 broadband radiative models. *Solar Energy*, 86(8):2145–2169. Progress in Solar Energy 3.

Gueymard, C. A. (2014). A review of validation methodologies and statistical performance indicators for modeled solar radiation data: Towards a better bankability of solar projects. *Renewable and Sustainable Energy Reviews*, 39:1024–1034.

Habte, A., Sengupta, M., and Lopez, A. (2017). Evaluation of the national solar radiation database (NSRDB version 2): 1998–2015. Technical report, NREL. Task No. ST6S.0810.

Hu, X., Eichner, J., Gong, D., Barreiro, M., and Kantz, H. (2022). Combined impact of ENSO and Antarctic Oscillation on austral spring precipitation in Southeastern South America (SESA). *Climate Dynamics*.

Ineichen, P. (2014). Long term satellite global, beam and diffuse irradiance validation. *Energy Procedia*, 48:1586–1596. Proceedings of the 2nd International Conference on Solar Heating and Cooling for Buildings and Industry (SHC 2013).

Ineichen, P. (2016). Validation of models that estimate the clear sky global and beam solar irradiance. *Solar Energy*, 132:332–344.

Laguarda, A. (2021). *Modelado de la irradiancia solar sobre la superficie terrestre: Modelos físicos e híbridos utilizando información satelital sobre la Pampa Húmeda*. PhD thesis, Facultad de Ingeniería, Universidad de la República. Tesis de Doctorado en Ingeniería de la Energía.

Laguarda, A. and Abal, G. (2020). Impacto de la incertidumbre de las variables atmosféricas de la base MERRA-2 en el modelado de la irradiancia solar en cielo despejado. *AVERMA Avances en Energías Renovables y Medio Ambiente*, 24:212–221.

Laguarda, A., Giacosa, G., Alonso-Suárez, R., and Abal, G. (2020). Performance of the site-adapted CAMS database and locally adjusted cloud index models for estimating global solar horizontal irradiation over the Pampa Húmeda region. *Solar Energy*, 199:295–307.

Laguarda, A., Iturbide, P., Orsi, X., Denegri, M. J., Luza, S., Burgos, B. L., Stern, V., and Alonso-Suárez, R. (2021). Validación de modelos satelitales heliosat-4 y CIM-ESRA para la estimación de irradiancia solar en la Pampa Húmeda. *Energías Renovables y Medio Ambiente (ERMA)*, 48:1–9.

Lefèvre, M., Oumbe, A., Blanc, P., Espinar, B., Qu, Z., Wald, L., Homscheidt, M. S., and Arola, A. (2013). McClear: a new model estimating downwelling solar radiation at ground level in clear-sky conditions. *Atmospheric Measurement Techniques, European Geosciences Union*, 6:2403–2418.

Liu, B. and Jordan, R. (1960). he interrelationship and characteristic distribution of direct, diffuse and total solar radiation. *Solar Energy*, 4(3).

Long, C. and Shi, Y. (2008). An automated quality assessment and control algorithm for surface radiation measurements. *The Open Atmospheric Science Journal*, 2:23–37.

Maxwell, G., WIlcox, S., and Rymes, M. (1993). *Users Manual for SERI QC Software, Assessing the Quality of Solar Radiation Data*. National Renewable Energy Laboratory (NREL), Golden, Colorado.

Mayer, B. and Kylling, A. (2005). Technical note: The libRadtran software package for radiative transfer calculations – description and examples of use. *Atmospheric Chemistry and Physics*, 5:1855–1877.

McArthur, L. (2005). Baseline surface radiation network operations manual. Technical Report WCRP-121/ WMO TD-No. 1274, WORLD CLIMATE RESEARCH PROGRAMME - WMO.

Nonnenmacher, L., Kaur, A., and Coimbra, C. (2014). Verification of the SUNY direct normal irradiance model with ground measurements. *Solar Energy*, 99:246–258.

Oumbe, A., Qu, Z., Blanc, P., Lefèvre, M., Wald, L., and Cros, S. (2014). Decoupling the effects of clear atmosphere and clouds to simplify calculations of the broadband solar irradiance at ground level. *Geoscientific Modeel Development*, 7:1661–1669.

Peel, M. C., Finlayson, B. L., and Mcmahon, T. A. (2007). Updated world map of the köppen-geiger climate classification. *Hydrology and Earth System Sciences Discussions*, 11:1633–1644.

Perez, R., Ineichen, P., Moore, K., Kmiecik, M., Chain, C., George, R., F., and Vignola (2002). A new operational model for satellite-derived irradiances: description and validation. *Solar Energy*, 73:307–317.

Perez, R., Ineichen, P., Seals, R., and Zelenka, A. (1990). Making full use of the clearness index for parameterizing hourly insolation conditions. *Solar Energy*, 45(2):111–114.

Perez, R., Schlemmer, J., Hemker, K., Kivalov, S., Kankiewicz, A., and Gueymard, C. (2015). Satellite-to-irradiance modeling - a new version of the SUNY model. In *42nd Photovoltaic Specialist Conference (PVSC)*, pages 1–7.

Porfirio, A. C. S. and Ceballos, J. (2017). A method for estimating direct normal irradiation from GOES geostationary satellite imagery: Validation and application over Northeast Brazil. *Solar Energy*, 155:178–190.

Qu, Z., Oumbe, A., Blanc, P., Espinar, B., Gesell, G., Gschwind, B., Klüser, L., Lefèvre, M., Saboret, L., Schroedter-Homscheidt, M., and Wald, L. (2017). Fast radiative transfer parameterisation for assessing the surface solar irradiance: The Heliosat-4 method. *Meteorologische Zeitschrift*, 26(1):33–57.

Rigollier, C., Bauer, O., and Wald, L. (2000). On the clear sky model of the ESRA — European Solar Radiation Atlas — with respect to the Heliosat method. *Solar Energy*, 68(1):33–48.

Rigollier, C., Lefevre, M., and Wald, L. (2004). The method Heliosat-2 for deriving shortwave solar radiation from satellite images. *Solar Energy*, 77(2):159–169.

Ruiz-Arias, J., Alsamamra, H., Tovar-Pescador, J., and Pozo-Vázquez, D. (2010). Proposal of a regressive model for the hourly diffuse solar radiation under all sky conditions. *Energy Conversion and Management*, 51:881–893.

Ruiz-Arias, J. A. and Gueymard, C. A. (2018). A multi-model benchmarking of direct and global clear-sky solar irradiance predictions at arid sites using a reference physical radiative transfer model. *Solar Energy*, 171:447–465.

Sengupta, M., Habte, A., Gotseff, P., Weekley, A., A., L., Anderberg, M., C., M., and Heidinger, A. (2014a). A physics-based GOES product for use in NREL's national solar radiation database. Conference paper NREL/CP-5D00-62776, NREL.

Sengupta, M., Habte, A., Gotseff, P., Weekley, A., A, L., C., M., and Heidinger, A. (2014b). A physics-based GOES product for use in NREL's national solar radiation database. Conference paper NREL/CP-5D00-62237, NREL.

Sengupta, M., Xie, Y., Lopez, A., Habte, A., Maclaurin, G., and Shelby, J. (2018). The National Solar Radiation Data Base (NSRDB). *Renewable and Sustainable Energy Reviews*, 89:51–60.

Tarpley, J. (1979). Estimating incident solar radiation at the surface from geostationary satellite data. *Journal of Applied Meteorology*, 18(9):1172–1181.

Xie, Y., Sengupta, M., and Dudhia, J. (2016). A fast all-sky radiation model for solar applications (FARMS): Algorithm and performance evaluation. *Solar Energy*, 135:435–445.

Xie, Y., Sengupta, M., Liu, Y., Long, H., and Habte, A. (2020). Progress on the National Solar Radiation Data Base (NSRDB): A new DNI computation. *IEEE Xplore*, pages 330–332.